

X-RAY LIGHT CURVES OF GAMMA-RAY BURSTS DETECTED WITH THE ALL-SKY MONITOR ON *RXTE*D. A. SMITH<sup>1</sup>, A. LEVINE<sup>2</sup>, H. BRADT<sup>2,3</sup>, K. HURLEY<sup>4</sup>, M. FEROCI<sup>5</sup>, P. BUTTERWORTH<sup>6,7</sup>, S. GOLENETSKII<sup>8</sup>, G. PENDLETON<sup>9,10</sup>, & S. PHENGCHAMNAN<sup>10</sup>  
donaldas@umich.edu

Draft: October 25, 2018

## ABSTRACT

We present X-ray light curves (1.5–12 keV) for fifteen gamma-ray bursts (GRBs) detected by the All-Sky Monitor on the *Rossi X-ray Timing Explorer*. We compare these soft X-ray light curves with count rate histories obtained by the high-energy ( $> 12$  keV) experiments BATSE, *Konus-Wind*, the *BeppoSAX* Gamma-Ray Burst Monitor, and the burst monitor on *Ulysses*. We discuss these light curves within the context of a simple relativistic fireball and synchrotron shock paradigm, and we address the possibility of having observed the transition between a GRB and its afterglow. The light curves show diverse morphologies, with striking differences between energy bands. In several bursts, intervals of significant emission are evident in the ASM energy range with little or no corresponding emission apparent in the high-energy light curves. For example, the final peak of GRB 970815 as recorded by the ASM is only detected in the softest BATSE energy bands. We also study the duration of bursts as a function of energy. Simple, singly-peaked bursts seem consistent with the  $E^{-0.5}$  power law expected from an origin in synchrotron radiation, but durations of bursts that exhibit complex temporal structure are not consistent with this prediction. Bursts such as GRB 970828 that show many short spikes of emission at high energies last significantly longer at low energies than the synchrotron cooling law would predict.

*Subject headings:* gamma rays: bursts

## 1. INTRODUCTION

1.1. *X-Rays from Gamma-Ray Bursts*

The first detection of a gamma-ray burst (GRB) at X-ray energies ( $\sim 1$ –15 keV) was made in 1972 with two proportional counters on the *OSO-7* satellite (Wheaton et al. 1973). For the next 15 years, there were few X-ray observations of GRBs, but they showed that the investigation of a new region of the spectrum could reveal interesting GRB properties. Instruments on *Apollo-16* were used to detect a GRB, also in 1972, and light curves in several energy bands showed that the spectrum evolved over the burst's single peak (Metzger et al. 1974; Trombka et al. 1974). Four bursts were detected with the Air Force satellite *P78-1* in 1979, and the peak X-ray emission was found to lag the peak gamma-ray emission (Laros et al. 1984).

Analysis of  $\sim 150$  bursts detected by the *Konus* instruments on *Venera 11* and *Venera 12* showed spectral evolution to be the rule rather than the exception (Mazets et al. 1981). Golenetskii et al. (1983) found that the spectral evolution of a small sample of GRBs could be characterized in terms of a hardness–intensity correlation. Later, Norris et al. (1986) reported a tendency for high-energy emis-

sion to lead the low-energy emission in bursts detected by instruments on the *Solar Maximum Mission* satellite. Ford et al. (1995) extended the study of spectral evolution to BATSE observations of GRBs and found that the peak energy of the spectral distribution increases concurrently with or slightly ahead of major increases in source intensity. They also found that when multiple peaks are present, later peaks tend to be softer than earlier peaks. A more extensive discussion of spectral evolution in GRBs may be found in Lloyd & Petrosian (2000).

Studies of X-ray counterparts to GRBs intensified in the late 1980s. The *Ginga* satellite was equipped with co-aligned wide-field detectors to cover the energy range from 2–400 keV (Murakami et al. 1989). These instruments were used to detect  $\sim 120$  bursts between 1987 and 1991 (Ogasaka et al. 1991). Analysis of twenty-two of these observations confirmed that spectral softening is common in the tails of bursts and showed that the X-ray band can contain a large fraction of the energy emitted from a GRB (Strohmayer et al. 1998). X-ray precursors were observed in a few cases (Murakami et al. 1991). Between 1989 and 1994, 95 bursts were detected by the GRANAT/WATCH all-sky monitor in two energy

<sup>1</sup> The University of Michigan, Ann Arbor, MI, 48109

<sup>2</sup> Center for Space Research, Massachusetts Institute of Technology, Cambridge, MA, 02139

<sup>3</sup> Department of Physics, Massachusetts Institute of Technology, Cambridge, MA, 02139

<sup>4</sup> Space Sciences Laboratory, University of California, Berkeley, CA, 94720

<sup>5</sup> Istituto de Astrofisica Spaziale (CNR), 00133, Rome Italy

<sup>6</sup> NASA/Goddard Space Flight Center, Greenbelt, MD, 20771

<sup>7</sup> Emergent Information Technologies, Largo, MD, 20774

<sup>8</sup> Ioffe Physico-Technical Institute, Russian Academy of Sciences, St. Petersburg, 194021, Russia

<sup>9</sup> COLSA Corporation, Huntsville, AL, 35806

<sup>10</sup> Department of Physics, University of Alabama, Huntsville, AL, 35899

bands, 8–20 keV and 20–60 keV, and thirteen of them were found to exhibit significant emission in the lower energy band before and/or after the activity in the higher energy band (Sazonov et al. 1998).

The Wide Field Camera on *BeppoSAX* was used to detect 45 GRBs in the 1.5–26.1 keV band between July 1996 and February 2001<sup>11</sup>. Only one of those bursts (GRB 980519) exhibited significant soft X-ray activity before the onset of the GRB in gamma-rays (in ‘t Zand et al. 1999). In addition to providing broadband light curves for these GRBs (Frontera et al. 2000), the *BeppoSAX* effort has revealed the existence of GRB “afterglows”, the fading emission sometimes seen after a GRB (Costa et al. 1997).

The general picture that has emerged is that X-ray light curves for GRBs tend to track their gamma-ray counterparts. Spectral evolution may or may not be present. Most often the times of X-ray peak emission tend to lag behind the peaks at higher energies. Bursts tend to last longer in X-rays, but this is not true of every burst. A small fraction of bursts exhibit X-ray activity with no corresponding emission at high energies. This X-ray activity sometimes precedes the gamma-ray burst proper and sometimes follows it. In very rare cases, it does both.

### 1.2. A Simplified Conventional Model

Piran (1999) has reviewed the standard “fireball” model for GRBs in great detail. We present a brief summary of this model, to which we shall refer when interpreting features of GRB light curves. In this model a large amount of energy ( $\sim 10^{51}$  ergs) is released into a small volume to create a very hot, optically thick fireball (Goodman

1986). The fireball expands rapidly, and since it contains only a very small amount of baryonic matter (Shemi & Piran 1990; Kobayashi et al. 1999), the expansion becomes highly relativistic (Blandford & McKee 1976). By the end of the acceleration phase, all the available energy has been transferred to the bulk kinetic flow (Cavallo & Rees 1978).

The optical depth of an expanding fireball,  $\tau$ , can be related to the bulk Lorentz factor of the expansion,  $\Gamma$ , and the minimum observed timescale for variability during the burst,  $\delta T$  (*e.g.* Piran (1999)). This relation hinges on the observation that high-energy GRB spectra are non-thermal, with a photon index  $\alpha$  ( $dN/dE \propto E^{-\alpha}$ ). In order for the observed spectrum to be non-thermal, the optical depth must be less than unity. The derived relation is

$$\tau \sim \frac{2 \times 10^{15}}{\Gamma^{4+2\alpha}} E_{52} \left( \frac{\delta T}{10 \text{ ms}} \right)^{-2} \lesssim 1, \quad (1)$$

where  $E_{52}$  is the total energy in the fireball in units of  $10^{52}$  ergs. This constraint demands a lower limit on the bulk Lorentz factor, dependent on  $\alpha$ . Early work found that the high energy spectral index can vary from  $\sim 1.6$  to higher than 5, with no particular preferred value (Band et al. 1993). A recent analysis of bright bursts from the Fourth BATSE Catalog reports an asymmetric distribution of high-energy spectral indices that peaks around 2.25 and extends beyond 4 (Preece et al. 2000). If  $\alpha$  is 2.25, and the other terms in Equation 1 are of order unity, then  $\Gamma$  must be greater than  $\sim 60$ .

Once such a highly relativistic speed is reached, the ejecta coast quietly until one of two kinds of shocks form. When the ejecta sweep up mass from the surrounding

<sup>11</sup> See also J. Greiner’s archive at <http://www.aip.de:8080/~jcg/grbgen.html>

TABLE 1  
BURST TIMES AND LOCATIONS

Date of GRB (yymmdd)	Time of GRB (hh:mm:ss)	Confirming Satellite <sup>a</sup>	R.A. (J2000)	Decl. (J2000)
960416	04:09:00	ubk	04h15m27s	+77°10′
960529	05:34:34	k	02h21m50s	+83°24′
960727	11:57:36	uk	03h36m36s	+27°26′
961002	20:53:55	uk	05h34m46s	−16°44′
961019	21:08:11	ubk	22h49m00s	−80°08′
961029	19:05:10	k	06h29m27s	−41°32′
961216	16:29:02	bk	...	...
961230	02:04:52	u	20h36m45s	−69°06′
970815	12:07:04	ubks	16h08m33s	+81°30′
970828	17:44:37	ubki	18h08m23s	+59°19′
971024	11:33:32	bk	18h25m00s	+49°27′
971214	23:20:41	ubnks	12h04m56s	+64°43′
980703	04:22:45	ubk	23h59m04s	+08°33′
981220	21:52:21	uks	03h43m38s	+17°13′
990308	05:15:07	ubk	12h23m11s	+06°44′
000301C	09:51:39	unk	16h20m19s	+29°26′

<sup>a</sup>u - *Ulysses*; b - BATSE; k - Konus; s - *BeppoSAX*; n - *NEAR*; i - *SROSS-C*

medium, they decelerate and convert the bulk kinetic energy to random motion and radiation (Mészáros & Rees 1992; Rees & Mészáros 1992). This type of shock is referred to as “external”. If the central engine of the GRB source is erratic and emits multiple shells of ejecta at different speeds, “internal” shocks may form as these shells overtake each other, and radiation will be emitted (Kobayashi et al. 1997). The fading afterglow observed after many GRBs is believed to originate in the cooling of the material behind the external shock front (Mészáros & Rees 1997), while the complex temporal structure of the GRBs themselves has been attributed to multiple internal shocks (Narayan et al. 1992; Fenimore, Madras, & Nayakshin 1996). In both internal and external shocks, synchrotron emission is expected to be the dominant source of radiation (Sari et al. 1996; Piran 1999), although internal shocks are expected to be more efficient (Sari & Piran 1997; Kobayashi et al. 1997; Kobayashi & Sari 2001).

In a model of post-shock synchrotron radiation, the frequency of peak emission ( $\nu_m$ ) increases as the bulk Lorentz factor of the shock ( $\Gamma_{\text{sh}}$ ) to the fourth power (Sari et al. 1996, 1998; Wijers & Galama 1999). The inverse of this relationship is given by

$$\Gamma_{\text{sh}} = 14 \epsilon_B^{-1/8} \epsilon_e^{-1/2} n_1^{-1/8} \left( \frac{p-1}{p-2} \right)^{1/4} \left( \frac{h\nu_m}{1 \text{ keV}} \right)^{1/4} \quad (2)$$

(see, *e.g.*, Piran (1999), Equation 105), where  $n_1$  is the density of the external medium in  $\text{cm}^{-3}$ ,  $\epsilon_B$  and  $\epsilon_e$  define the fractional energy transferred to the post-shock magnetic field and electron distribution, respectively, and  $p$  is the index of the number spectrum of the Lorentz factor

distribution of the shocked electrons ( $N(> \Gamma_{\text{sh}}) \propto \Gamma_{\text{sh}}^{-p}$ ).

In this paper we present X-ray light curves for the GRBs detected with the All-Sky Monitor (ASM) on the *Rossi X-ray Timing Explorer* (RXTE) and interpret them in the context of this synchrotron shock model. These light curves are for the GRBs described in Smith et al. (1999), to which we add those for GRB 990308 and GRB 000301C. We also present a light curve for GRB 961216, which was detected but could not be localized accurately. All these events have been confirmed as GRBs via their detection at higher energies by other instruments in the Interplanetary Network (Table 1)<sup>12</sup>. Satellites participating in the IPN during the time interval covered by this work include *CGRO*, *Wind*, *SROSS-C*, *NEAR*, *BeppoSAX*, and *Ulysses*. Section 2 describes the data and our analysis techniques. Section 3 presents the observations and the GRB light curves. We compare the ASM light curves with the associated high-energy light curves recorded by detectors on other satellites. Section 4 summarizes both the common features and the striking differences among these light curves and discusses them in the context of the model.

## 2. INSTRUMENTATION AND ANALYSIS

The ASM consists of three Scanning Shadow Cameras (SSCs) mounted on a motorized rotation drive (Levine et al. 1996). The assembly holding the three SSCs is generally held stationary for a 90-s “dwell”. The drive rotates the SSCs through 6° between dwells, except when it is necessary to rewind the assembly. Each SSC contains a proportional counter with eight resistive anodes and views

<sup>12</sup> A list of burst detections by the IPN is maintained by K. Hurley at <http://ssl.berkeley.edu/ipn3/>.

TABLE 2  
BURST FLUXES AND FLUENCES

Date of GRB (yyymmdd)	1.5–12 keV Fluence <sup>a</sup> ( $10^{-7}$ ergs $\text{cm}^{-2}$ )	50–200 keV Fluence <sup>b</sup> ( $10^{-7}$ ergs $\text{cm}^{-2}$ )	1.5–12 keV Peak Flux <sup>a</sup> ( $10^{-8}$ ergs $\text{cm}^{-2}$ $\text{s}^{-1}$ )
960416	$6.0 \pm 0.3$	8.0	$7.8 \pm 0.8$
960529	$> 17.5 \pm 0.6$	58	$2.2 \pm 0.2$
960727	$9.5 \pm 0.5$	84	$6.0 \pm 0.5$
961002	$9.2 \pm 0.5$	35	$7.1 \pm 0.6$
961019	$4.6 \pm 0.6$	14	$3.1 \pm 0.7$
961029	$> 3.3 \pm 0.4$	20	$> 3.2 \pm 0.5$
961216	...	12	...
961230	$1.5 \pm 0.3$	...	$0.65 \pm 0.08$
970815	$> 33.3 \pm 0.8$	80	$6.1 \pm 0.5$
970828	$> 14.9 \pm 0.6$	280	$4.0 \pm 0.5$
971024	$> 1.1 \pm 0.3$	40	$0.4 \pm 0.1$
971214	$3.4 \pm 0.3$	36	$0.9 \pm 0.2$
980703	$> 18.3 \pm 0.8$	72	$3.2 \pm 0.3$
981220	$12.6 \pm 0.5$	52	$8.2 \pm 0.9$
990308	$5.8 \pm 0.4$	18	$1.3 \pm 0.3$
000301C	$3.8 \pm 0.5$	16	$4.7 \pm 0.9$

<sup>a</sup>75.5 c/s in ASM units  $\equiv$  1 Crab  $\equiv 2.8 \times 10^{-8}$  erg  $\text{cm}^{-2}$   $\text{s}^{-1}$

<sup>b</sup>Derived from Konus observations

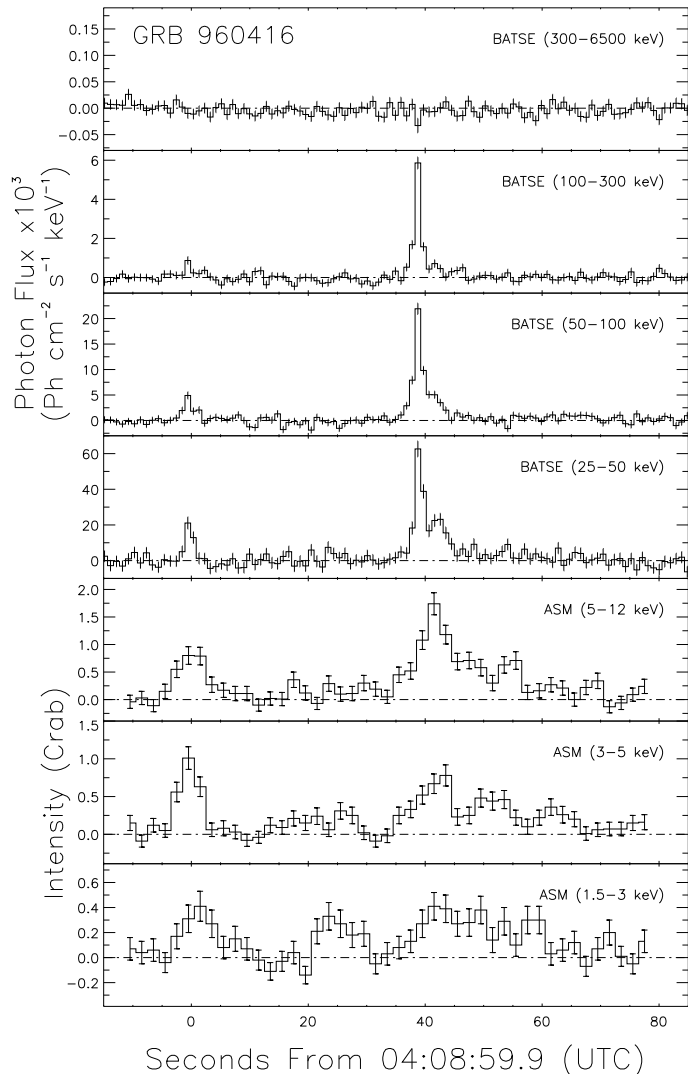


Fig. 1 – Time-series data for GRB 960416 in six energy channels as recorded by both the ASM (2-s bins; 1.5–12 keV) and BATSE (1-s bins; 25–6500 keV). The ASM light curve is the weighted average of measurements by both SSC 1 and SSC 2. Where possible, the ASM light curves presented in these figures have been converted into Crab flux units by the method described in Section 2.

a  $12^\circ \times 110^\circ$  (FWZI) field through a mask perforated with pseudo-randomly spaced slits. The long axes of the slits run perpendicular to the anodes. The net effective area for a source at the center of the FOV is  $\sim 30 \text{ cm}^2$ .

During each dwell, the positions of incident photons are tabulated in histograms for each anode for each of three pulse height channels: 1.5–3, 3–5, and 5–12 keV, denoted A, B, and C, respectively. The logical union of these three bands is referred to as the “sum band”, or “S”. In this position histogram mode, the arrival time of each photon is not preserved. A histogram contains information on the pattern of illumination of the detector through the slit mask from each discrete X-ray source in the field of view (FOV), as well as contributions from the diffuse X-ray background and local particle events.

For each of the three energy channels, we carry out a fit of these data to obtain the strength of each known X-ray

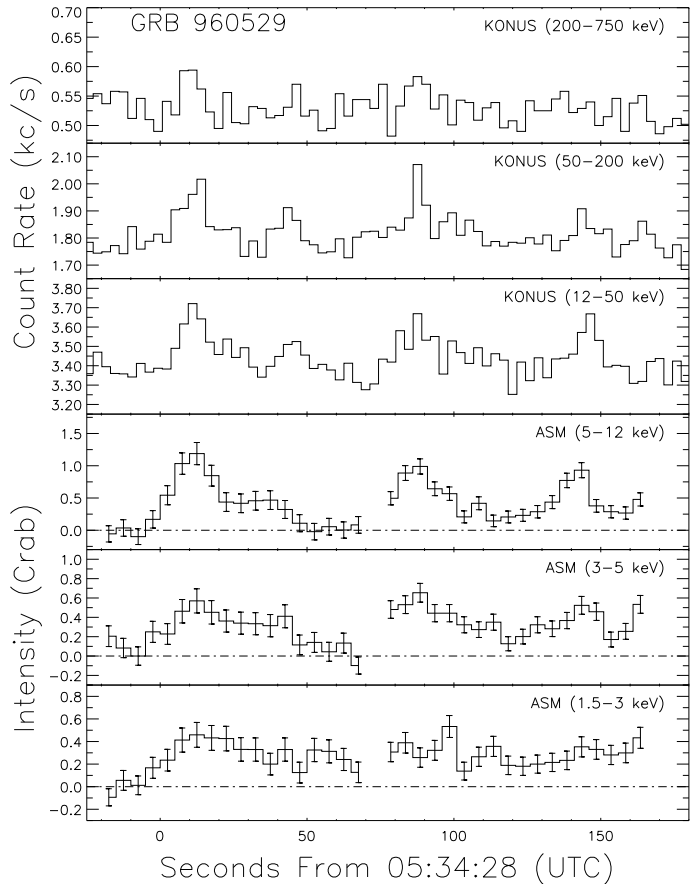


Fig. 2 – Time-series data for ASM and Konus observations of GRB 960529. The ASM light curve is the weighted average of measurements by both SSC 1 and SSC 2, in 5-s bins. A gap indicates the 6 s interval between dwells when the ASM assembly was in motion. The Konus count rates are from the “waiting-mode” data in 3-s bins.

source in counts per  $\sim 30 \text{ cm}^2$  for the entire 90-s dwell. Division by the exposure time and the application of a multiplicative correction factor yields the intensity in “ASM units”. The time-dependent correction factor ( $\equiv a$ ) is empirically determined such that the corrected intensity of the Crab Nebula is the count rate that would be obtained for the source had it been at the center of the FOV of SSC 1 at a fiducial time near the start of the mission. The ASM units for 1.0 Crab are 26.8, 23.3, 25.4, and 75.5 counts  $\text{s}^{-1}$  for the A, B, C, and Sum channels respectively. Table 2 shows the burst fluences and peak fluxes as measured by the ASM in the Sum band. ASM units are converted to physical units by assuming a Crab-like spectrum (Seward 1978) in the 1.5–12 keV band, which yields an integrated flux of  $2.8 \times 10^{-8} \text{ erg cm}^{-2} \text{ s}^{-1}$ .

A second data mode records the total number of 1.5–12 keV events detected from all sources in the FOV of each SSC. These data are recorded in 0.125-s bins in each of the same three energy channels as the position histogram mode. In this “multiple time series” (MTS) data mode, the physical location in the detector of each incident photon is not preserved.

In combination, these two data modes can yield a light curve for a highly variable source like a GRB. The

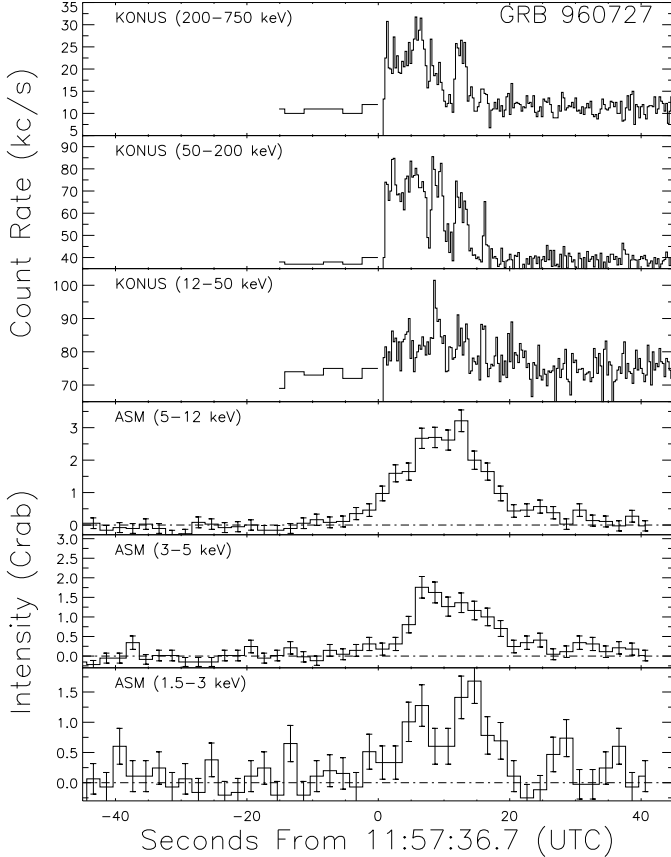


Fig. 3 – ASM time-series data from SSC 2 for GRB 960727 (2-s bins) in three energy bands, as well as the corresponding count rate histories from Konus (0.25-s bins after the trigger) in three energy bands.

challenge these data present is to properly set the background level in the MTS data. We take advantage of the fact that no known variable X-ray sources were in the FOV during the observations of any of the GRBs presented here and assume that the count rates from all sources other than the GRB do not vary during the dwell. Should the FOV contain variable sources other than the GRB, or should the background rate vary, the method described here would be invalid. The total number of counts from the GRB source detected during one dwell of one SSC is obtained from the standard fit to the position histogram data. We then define the effective background level (for the GRB) in the MTS count rate data such that the total number of counts above that level for the appropriate 90-s interval is equal to the number of counts inferred from the position histogram data to come from the GRB source. The number of MTS counts from the GRB recorded in a given time bin can therefore be estimated as:

$$c_j = n_j - t_j \left( \frac{N}{T} - \frac{fR}{a} \right), \quad (3)$$

where the term in parentheses is the inferred background rate.  $N$  is the total number of MTS counts detected in a given SSC energy band during an observation with total exposure time  $T$ ,  $R$  is the time-averaged GRB source intensity in ASM units derived from the fit to the position-histogram data,  $f$  is the transmission fraction for the location of the GRB in the FOV,  $a$  is the time-dependent

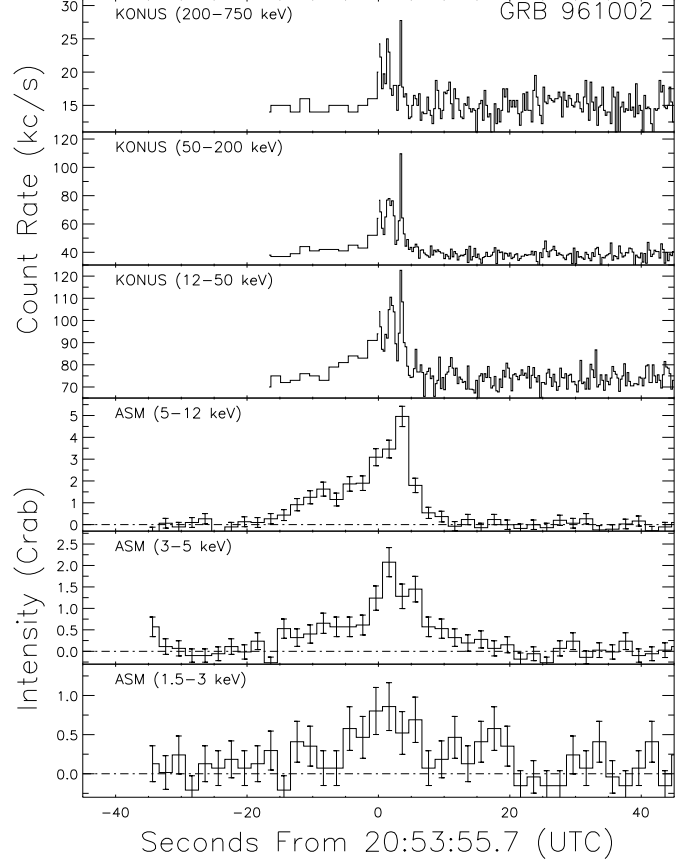


Fig. 4 – ASM time-series data from SSC 2 for GRB 961002 (2-s bins) in three energy bands, as well as the corresponding count rate histories from Konus (0.25-s bins after the trigger) in three energy bands.

correction factor,  $t_j$  is the time bin size in seconds, and  $n_j$  is the number of counts in the  $j$ th time bin. One can then convert  $c_j$  into ASM units through multiplication by  $a/f$ . For additional details see Smith (1999).

We compare the resulting ASM light curves with available contemporaneous BATSE, *Ulysses*, Konus, or *Bep-poSAX* GRBM count rates. The BATSE count rates shown here are extracted from the `discsc` mode FITS files and converted to photon flux rates according to the method described in Pendleton et al. (1994, 1996, 1997). This method combines a photon spectral model with a coarse spectral inversion technique. A polynomial defined in Log photon energy – Log photon flux across the four broad energy bins is used as the spectrum to construct the detector response matrix (DRM) prior to the application of a direct spectral inversion technique. The first inversion yields a preliminary coarse photon spectrum that is used to re-evaluate the coefficients of the GRB's spectral polynomial. This updated polynomial is used to build a second DRM employed in a second application of the spectral inversion technique that produces the final photon flux data. The data produced with this method are also used to generate the BATSE GRB peak flux data for the BATSE burst catalogs. These data are presented in four energy channels with nominal energy ranges of 25–50, 50–100, 100–300, and 300–6500 keV. In one case (GRB 970828),

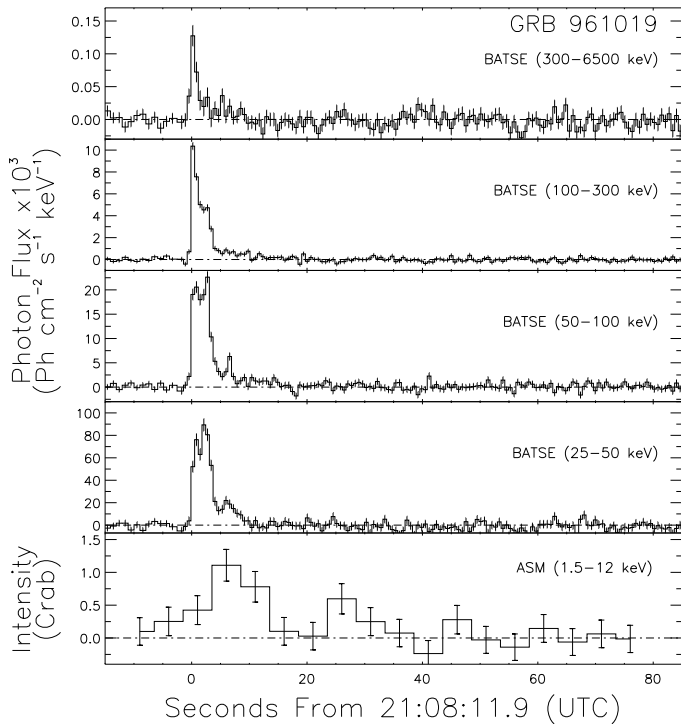


Fig. 5 – Time-series data from SSC 2 for GRB 961019 in both the ASM (5-s bins; 1.5–12 keV) and BATSE (0.64-s bins; 25–6500 keV).

the event occurred during a telemetry gap, so no `discsc` data were available. In this case, we used the 16-channel `MER` data and combined channels to approximate the energy ranges provided by the `discsc` mode. The conversion technique described above could not be applied to these data, so we present here the count rates without background subtraction.

Where BATSE data are not available, we compare the ASM light curves with the count rates from other high-energy instruments. The hard X-ray detectors for the solar X-ray/cosmic gamma-ray burst experiment on *Ulysses* record 25–150 keV photons in time bins of size between 0.25–2 s, depending on the telemetry rate available, switching to 0.03125-s bins on a trigger (Hurley et al. 1992). When the *BeppoSAX* GRBM registers a burst, the 40–700 keV count rate is stored in bins with a minimum size of 7.8 ms from 8 s before to 98 s after the trigger time; all on-board data is sent down once every  $\sim 90$ -min orbit for operators to examine (Frontera et al. 1997; Feroci et al. 1997). The *Konus* instrument on *Wind* records data continuously in a “waiting mode”, with bins of 2.9 s, but when a trigger is activated, counts are recorded in higher resolution for a certain amount of time after the trigger (Aptekar et al. 1995). The triggered data presented in this paper have been binned to 256 ms. Since *Konus* detected all but one of the GRBs presented here, the burst fluence as measured in the *Konus* 50–200 keV channel is presented in Table 2 to provide a consistent comparison with the 1.5–12 keV fluence as measured by the ASM. The times of the bins in the high energy light curves obtained from distant instruments such as *Ulysses* or *Konus* have been shifted to account for the propagation times. Light travel times between instruments in near Earth orbit are negligible.

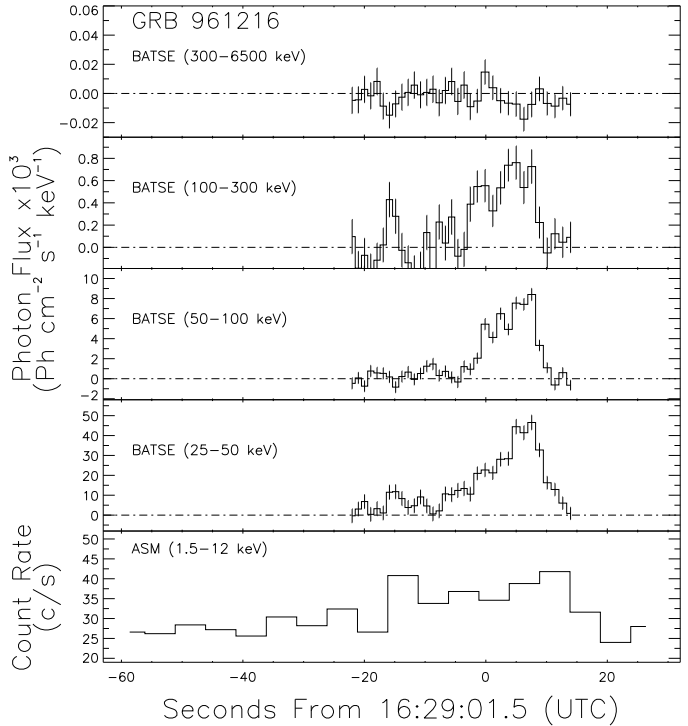


Fig. 6 – Time-series data from SSC 2 for GRB 961216 in both the ASM (5-s bins; 1.5–12 keV) and BATSE (1-s bins; 25–6500 keV). No background subtraction has been performed on the ASM data.

### 3. OBSERVATIONS

Smith et al. (1999) describe a search through 1.5 years of archived ASM time series data, as well as an ongoing program to scrutinize the ASM data on a near real-time basis for evidence of X-ray counterparts to GRBs. The near real-time program used three methods in conjunction: a low-threshold search for unidentified X-ray sources in ASM data around the times of bursts detected by BATSE or other IPN instruments, a search for variability in ASM MTS data, and examination of all ASM position histogram data for evidence of uncatalogued transient sources.

The efficiency of these searches for the detection of X-rays from GRBs depended on a number of factors. For any particular dwell, these included (1) the 2–12 keV peak flux and duration of the GRB, (2) the position of the GRB source within the field of view, (3) whether any other strong sources were in the field of view, and (4) the background level and variability, which often were affected because of passage through a region of high flux of energetic charged particles or because of contamination by scattered solar X-rays.

The variability search measured the deviations from a linear fit to the count rate over the given dwell. Thus, GRBs in which the X-ray flux changed slowly within the 90-s duration of a dwell were difficult to find. For example, if the ASM were to scan onto a slowly fading GRB in progress, the observation would not produce a substantial deviation from a linear trend, and would not be flagged in the variability search. We also ignored dwells with known strong sources in the FOV, because even if variability were

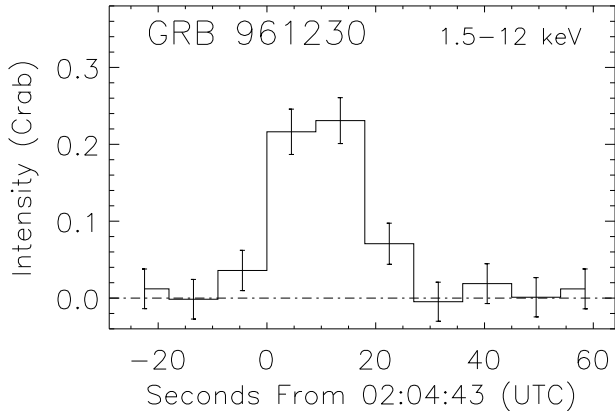


Fig. 7 – Time-series data for GRB 961230 (9-s bins; 1.5–12 keV), displaying the weighted average of measurements by both SSC 1 and SSC 2.

apparent, it would be difficult to determine the source of that variability.

We know of no bias against the detection of short GRBs in these searches, except that the shorter the duration of the X-ray event, the higher the peak flux must be to yield sufficient counts for the GRB to be detected in the position-histogram data. We found no ASM detections of any GRB counterparts which lasted less than a few seconds. Our results strongly suggest that short GRBs do not have X-ray fluences as high as those of longer GRBs.

As noted above, we searched for ASM counterparts of GRB events detected by BATSE and other high-energy instruments. We found no GRB event which is known through these other instruments to have occurred in the FOV of the ASM but was not detected. However, the localizations for most GRBs detected by higher energy instruments could not be constrained to lie completely within the ASM FOV.

Here we present, in chronological order, the ASM light curves for 15 of the GRBs discovered in these searches.

GRB 960416 (Fig. 1) was observed in both SSCs 1 and 2 during a single dwell. The BATSE light curve shows two distinct peaks  $\sim 40$  s apart. The two peaks are also seen in the ASM data, but the ASM reveals a third, remarkably soft, peak between them, as well as an extended tail for the final peak beyond the end of the BATSE event.

GRB 960529 (Fig. 2) exhibits three hard peaks in the ASM time-series data from two SSCs over the course of two successive dwells. Although no Konus trigger was explicitly activated, the waiting-mode data show the multi-peak structure of this burst out to 200 keV. The Konus light curve contains four major peaks, such that the extended tail of the first peak in the ASM light curve is resolved into two distinct peaks at higher energies.

GRB 960727 and GRB 961002 (Figs. 3 and 4) were each detected only in SSC 2. Each lasted about 30 s, and each showed a singly-peaked soft X-ray light curve without strongly significant structure on time scales down to  $\sim 1$  s. Neither burst was detected by BATSE, but each was detected by Konus and the GRB detector on *Ulysses*. The high-energy light curves reveal rich temporal structure. The ASM light curves do not show corresponding structure, but this is, at least in part, due to reduced sen-

sitivity to variability on subsecond time scales. Each event seems to conclude with a weak, extended X-ray tail, absent at high energies, that lasts for 10 or 20 s. The accuracy of the background estimation before the burst supports the existence of a post-burst X-ray excess, but the extended tail is too weak in the three ASM sub-bands to make a useful measurement of the energy-dependence of the decay rates.

GRB 961019 (Fig. 5) was detected in a single observation of SSC 2 and was also observed with BATSE. The BATSE light curve shows three sub-peaks. The GRB was only  $1^\circ.5 \pm 0.1$  from the edge of the SSC FOV, so that only 24% of the detector surface was exposed to the source. The X-ray peak emission may be delayed relative to the gamma-ray maximum by 5–10 s.

GRB 961029 (not shown) was detected as a dramatic rise in count rate only a few seconds from the end of a dwell. During this dwell, the source was located only  $2^\circ.0 \pm 0.2$  (Smith et al. 1999) from the edge of the FOV of SSC 2. As SSC 2 was rotated after the end of the dwell, the field of view moved off the direction to the GRB source and the signal was lost. Konus reported a burst detection at 19:05:10 (UTC), which is during the rise of the ASM event. No other high-energy GRB detector observed this event.

GRB 961216 (Fig. 6) was detected by a single SSC. The location of GRB 961216 lay only  $\sim 1^\circ$  from the edge of the FOV, which is outside the region for which our position-determining ability is well-calibrated (Smith et al. 1999). We therefore show the total 1.5–12 keV count rate as measured by the entire SSC without background subtraction.

GRB 961230 (Fig. 7) was a weak burst that was detected in both SSC 1 and SSC 2 during the same dwell. The X-ray flux lasted about 25 s and reached a peak of  $0.23 \pm 0.03$  Crab. This burst was detected by the GRB detector on *Ulysses* at 02:04:52 (UTC) but not by any other instrument.

GRB 970815 (Fig. 8) exhibited multiple peaks over an interval of several minutes. SSC 2 scanned onto the source during the decay from an initial peak. The decay timescale from this peak is clearly longer at lower energies, across all seven available energy channels, indicative of the spectral softening common to the early phases of GRB decay curves. A second peak began 70 s into the dwell, and a third peak  $\sim 50$  s after that, during the following dwell. The 90-s averaged flux from the GRB in the third dwell, during which the burst source was  $\sim 0^\circ.75$  from the edge of the FOV of SSC 1, is  $30 \pm 20$  mCrab (1.5–12 keV). Figure 9 shows the second peak on an expanded scale.

It is striking that the third peak, the strongest in the ASM light curve, barely registers in BATSE's two lowest energy channels (25–100 keV). The X-ray spectrum of the burst evolves rapidly during this peak, as indicated by a distinct soft lag of  $\sim 8$  s in the times of peak burst flux between the high and low energy channels of the ASM. The ASM spectrum during this peak is clearly different from that during the second peak. We assume a simple power law spectrum ( $N \propto E^{-s}$ ) without absorption in the 1.5–12 keV band and find the index  $s$  for the third peak is  $1.8 \pm 0.1$  while the second peak is harder, with an index of  $1.2 \pm 0.3$ . This change may also be described by a shift in the break frequency of the canonical, broken power-law,

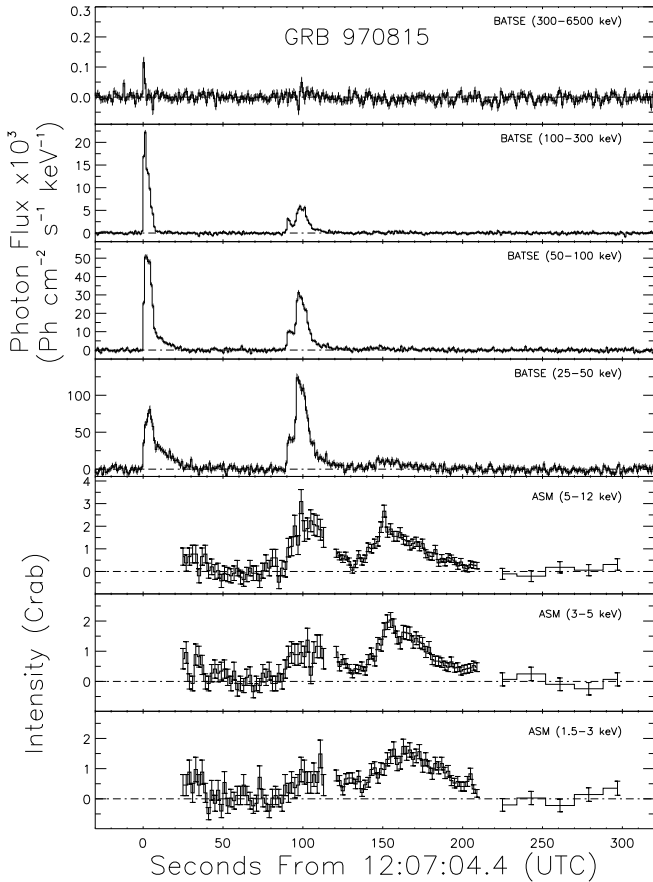


Fig. 8 – Light curves for GRB 970815 as measured by both the ASM and BATSE. The ASM scanned SSC 2 onto the GRB location during the decay of the first peak. Gaps in the ASM light curve indicate the 6 s intervals between dwells when the ASM assembly was in motion. The first two dwells are graphed in 2-s bins. The second dwell is represented here by the weighted average of SSCs 1 and 2. The GRB is very dim during the third dwell, and although the data from SSC 1 have been binned into 9-s bins, the flux in each bin is consistent with zero. The 90-s averaged flux from the GRB in this dwell is  $30 \pm 20$  mCrab (1.5–12 keV). The BATSE light curve is presented in 1-s bins (25–6500 keV).

“Band” spectrum. These indices were determined from a 5-s interval beginning 99 s after the BATSE trigger time and a 2-s interval beginning at 154 s.

GRB 970828 (Fig. 10) was a bright burst detected in both SSC 1 and 2 (Remillard et al. 1997). The burst onset was observed midway through a 90-s dwell. Its FOV location was such that it was only observed by SSC 1. The ASM drive assembly rotated the SSCs between dwells while the burst was still active, and the new aspect placed the burst’s FOV location just  $0^\circ.5$  inside the edge of the FOV of SSC 2. Despite the reduction in effective area, the counting rate during the second dwell yields a clear detection of the GRB in at least two of the three energy channels. A second rotation brought the source to the center of the FOV of SSC 2, in time to witness the final decay of the event. Spectral softening during this decay is apparent.

At the onset, the X-ray flux climbs more slowly than the gamma-ray flux, as shown in Figure 11, but the 5–12 keV

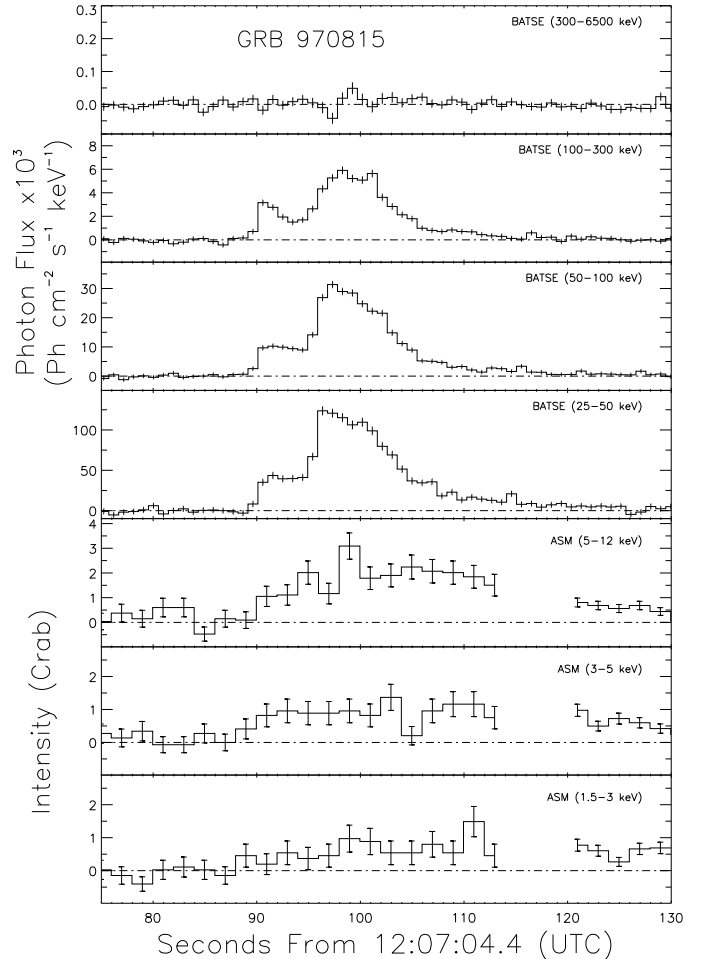


Fig. 9 – Light curves for GRB 970815 (Fig. 8) for the interval between 70 and 130 s after the BATSE trigger time, showing the second peak. There is a six-second gap at 114 s in the lower panels because the ASM assembly was in motion.

structure appears to echo the gamma rays. The time of peak emission may lag at lower X-ray energies. After 40 s, the high-energy flux drops below detectable levels, then subsequently flashes through at least five further peaks. Emission is detected by the ASM during the time interval around these peaks, but the counting statistics are too weak to allow the individual peaks to be resolved, even if they are present. The X-ray emission appears to last long after the cessation of gamma-ray activity.

GRB 971024 (Fig. 12) was an extremely weak burst in all energy bands. It was detected in both SSC 1 and SSC 2, but the latter yielded only an average flux over 90 s. Large systematic uncertainties in the estimation of the source flux stem from relatively large uncertainties in the source position (Smith et al. 1999). The BATSE light curves show obvious spectral softening over the  $\sim 110$  s of the decay, but the ASM light curve is too short and too weak for fruitful comparison.

GRB 971214 (Fig. 13) appeared as a moderate-intensity single-peak event, lasting  $\sim 40$  s, observed with SSC 3 during a single dwell. Limited statistics do not allow us to probe the soft X-ray light curve for counterparts to the complex structures in the BATSE hard X-ray data, *e.g.* the sharp spike at 32 s. As with GRB 970828, the



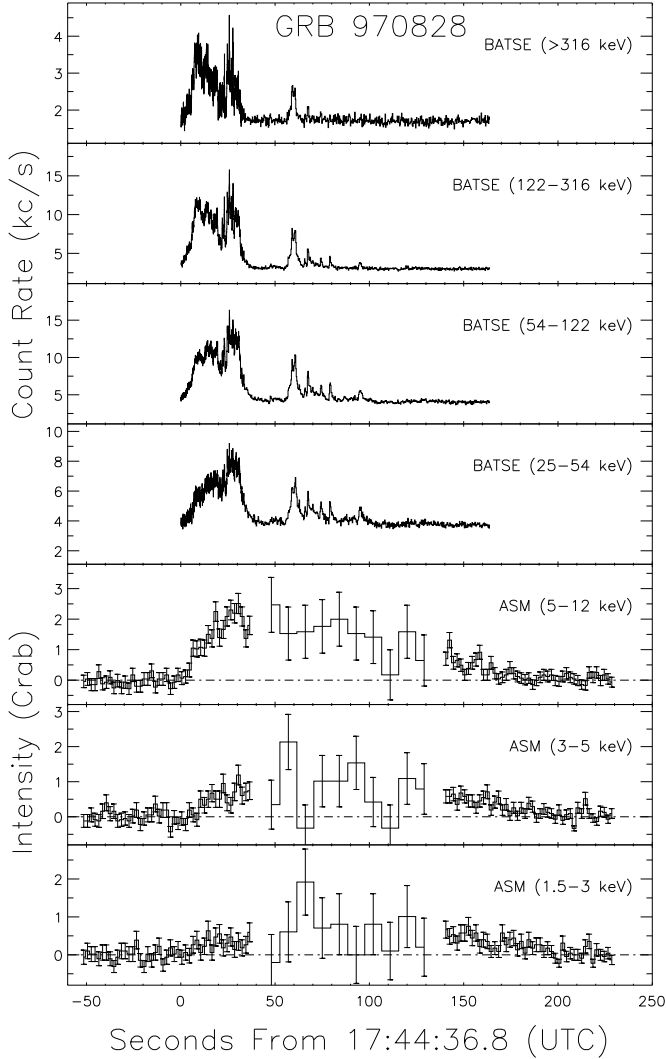


Fig. 10 – ASM time-series data in 2-s and 9-s bins for GRB 970828, compared with data from BATSE. The burst was first observed with SSC 1, and with SSC 2 during the second and third dwells.

duration of the X-ray event is longer than its gamma-ray counterpart.

GRB 980703 (Fig. 14) was detected in the FOVs of both SSCs 1 and 2 simultaneously. The flux rose over  $\sim 30$  s to reach a maximum measured value at the end of a 90-s dwell. The hard X-ray maximum, as measured by BATSE, leads the soft X-ray maximum by at least 6 s. The rising part of the burst is more variable at higher energies. During the second dwell, the GRB source is only  $0.6^\circ$  from the edge of the FOV of SSC 1 and is out of the FOV of SSC 2. Both BATSE and the ASM detect a lengthy tail. Since the transition from burst to tail in BATSE occurred while the ASM was in motion, we have no information on the X-ray properties of this transition.

GRB 981220 (Fig. 15) was observed in SSC 2 near the end of a 90-s dwell. This is the brightest GRB yet observed in the ASM data, reaching a flux of over 5 Crab in the Sum band (1.5–12 keV). Although this event was not observed by BATSE, it was observed in the GRBM on board *BeppoSAX*. The X-ray flux rises earlier than and

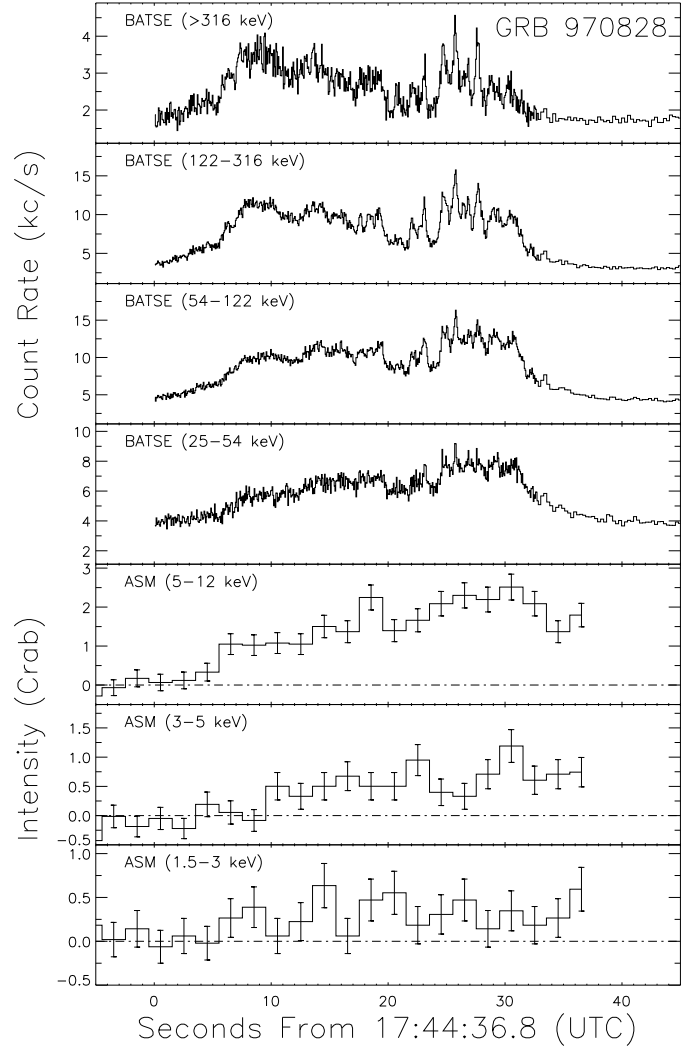


Fig. 11 – Light curves for GRB 970828 (Fig. 10) for the interval spanning 5 s before to 45 s after the BATSE trigger time. There is a six-second gap at 37 s in the lower panels because the ASM assembly was in motion.

declines after the gamma-ray event, and the spectrum softens during the decay.

GRB 990308 (Fig. 16) was observed in SSC 3 alone. An optical transient is associated with this burst (Schaefer et al. 1999), so the source position is accurately known. BATSE also detected this burst, and its count rate reveals a multiply-peaked light curve, some 35 s in duration. The soft X-ray light curve does not appear to last significantly longer than the hard X-ray light curve.

GRB 000301C (Fig. 17) was observed in SSC 2. It consisted of a single peak that reached over 3 Crab in the 5–12 keV band. No emission was detected in the 1.5–3 keV band, with a normalized  $2\sigma$  upper limit of 90 mCrab (integrated over 90-s). This burst was also detected by *Ulysses* and *NEAR* (Smith et al. 2000). The Earth lay between BATSE and the GRB at the time of the event (M. Kippen, private communication), and the *BeppoSAX* GRBM was powered down due to the passage of the satellite near the South Atlantic Anomaly.

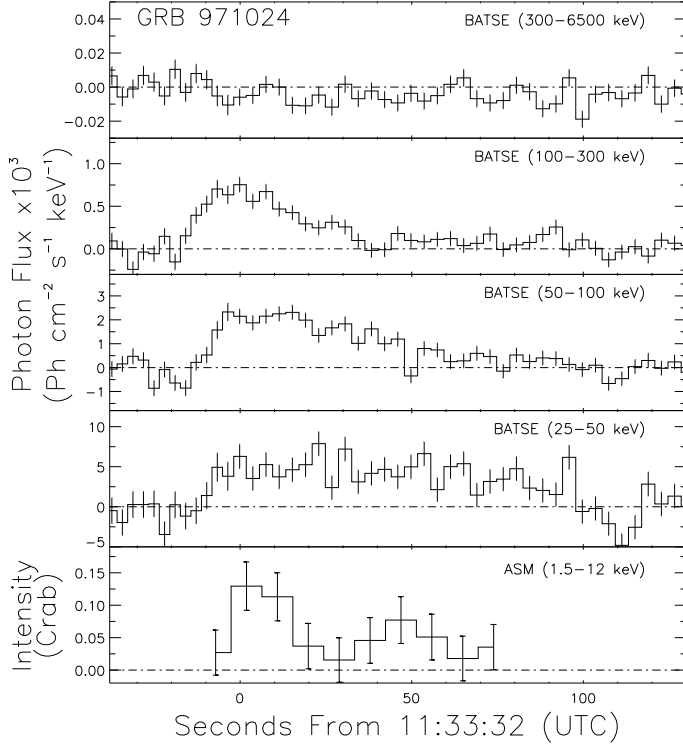


Fig. 12 – Time-series data for GRB 971024 in SSC 1 (9-s bins; 1.5–12 keV) and four BATSE energy bands (3.8-s bins).

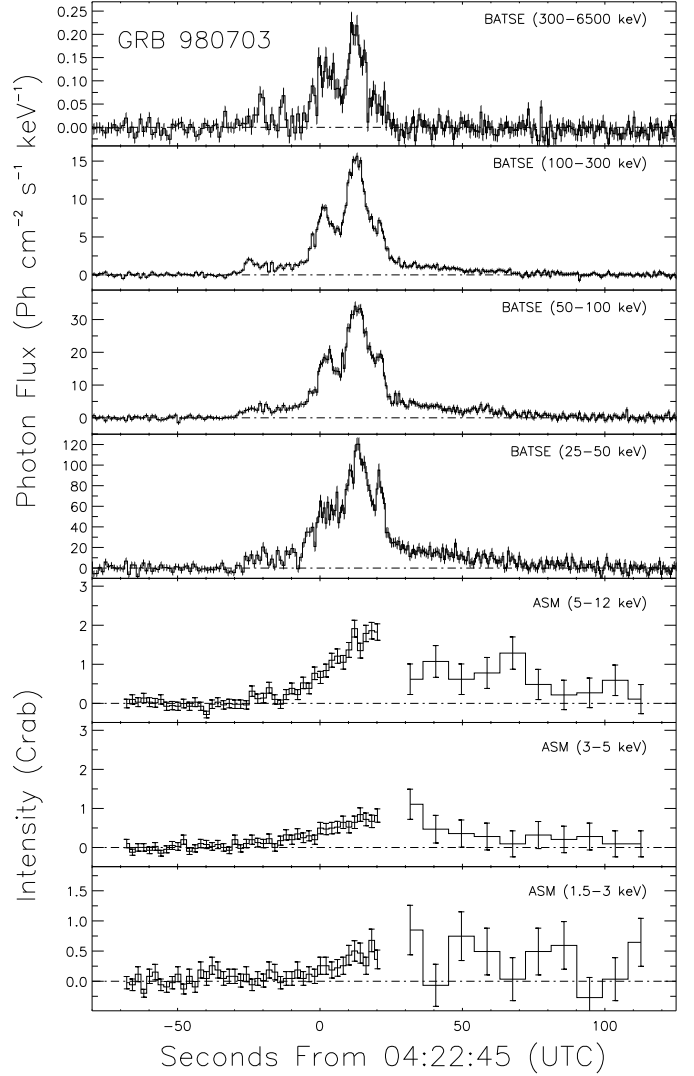


Fig. 14 – Time-series data for GRB 980703 both in SSC 1 and SSC 2 and later in SSC 1 alone (2-s and 9-s bins; 1.5–12 keV) and four BATSE energy channels (0.64-s bins after the trigger, 1-s bins before the trigger; 25–6500 keV).

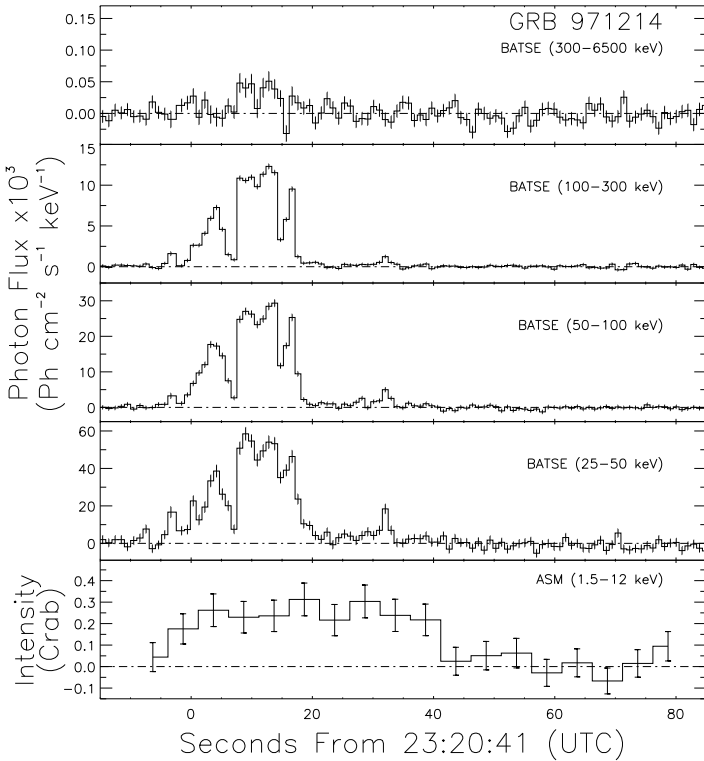


Fig. 13 – Time-series data for GRB 971214 in SSC 3 (5-s bins; 1.5–12 keV) and four BATSE energy bands (0.64-s bins).

#### 4. DISCUSSION

The external shock model has proven popular for explaining the major features of most GRB afterglow behavior, and the internal shock model has become the favored explanation for the temporal structure of the GRB itself. A clear observational distinction between the GRB event and afterglow remains elusive, although several candidate criteria have been proposed (Connors & Hueter 1998; Giblin et al. 1999; in 't Zand et al. 1999). In this section, we discuss the implications of these fifteen light curves for burst origins in the context of the simple model outlined in section 1.2. We discuss whether or not the observations are consistent with an origin in synchrotron radiation, and in three cases, we address the question of whether or not the ASM has observed the onset of the X-ray afterglow. A detailed analysis of spectral evolution in bursts observed with the ASM is beyond the scope of this paper.

The GRB light curves presented here are diverse in form. Very few of these bursts appear as simple fast-

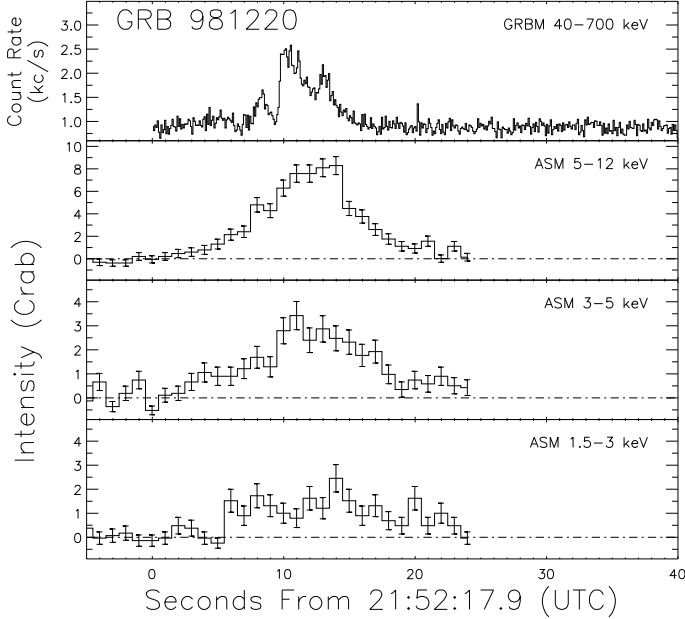


Fig. 15 – Time-series data (1.5–12 keV) for the ASM SSC 2 observation of GRB 981220 in 2 s bins and the count rate in the *BeppoSAX* GRB Monitor (40–700 keV). The spike at 20 s is an artifact.

rise, exponential-decay shapes that one might expect from impulsive events. In X-rays, several bursts show a near-symmetric single-peak (*e.g.* Fig. 15). Some bursts show significant structure on smaller time scales (*e.g.* Fig. 1), while others do not (*e.g.* Fig. 17). For many bursts, the substructure is an energy-dependent phenomenon (*e.g.* Figs. 2 and 14). Two bursts (Fig. 4 and 6) even seem to have a slow-rise, fast-decay structure! About half the bursts show multiple, distinct peaks, while five (Figs. 3, 4, 10, 13, and 16) have a veritable forest of peaks within their gamma-ray light curves.

Although each of these bursts shares some characteristics across the entire observed energy range, there are other features that are only detected in a few, or even one, energy channels. The second gamma-ray peak of GRB 960529 (Fig. 8) is smeared out at low energies and difficult to recognize as a distinct event. This smearing at low energies is common, and it can be seen in the onset of GRB 980703 (Fig. 14) as well as GRB 960727 (Fig. 3), GRB 961002 (Fig. 4), and GRB 981220 (Fig. 15). In contrast, GRB 960416 (Fig. 1) showed a peak unique to the softest ASM energy channels.

GRB 970815 (Fig. 8) shows multiple peaks, but in this case the last peak is unusually soft. An intriguing possibility is that the third peak is due to an external shock, and hence represents the beginning of the afterglow, while the first two peaks originate in internal shocks that occur before the outermost ejecta sweep up enough matter to instigate the external shock. It has been predicted that the afterglow could begin tens of seconds after the burst (Sari 1997; Sari & Piran 1999). We address the possibility that the ASM has detected the onset of X-ray afterglow emission by examining here the three bursts for which searches for X-ray afterglow were carried out hours after the event.

If the third peak in GRB 970815 does represent the on-

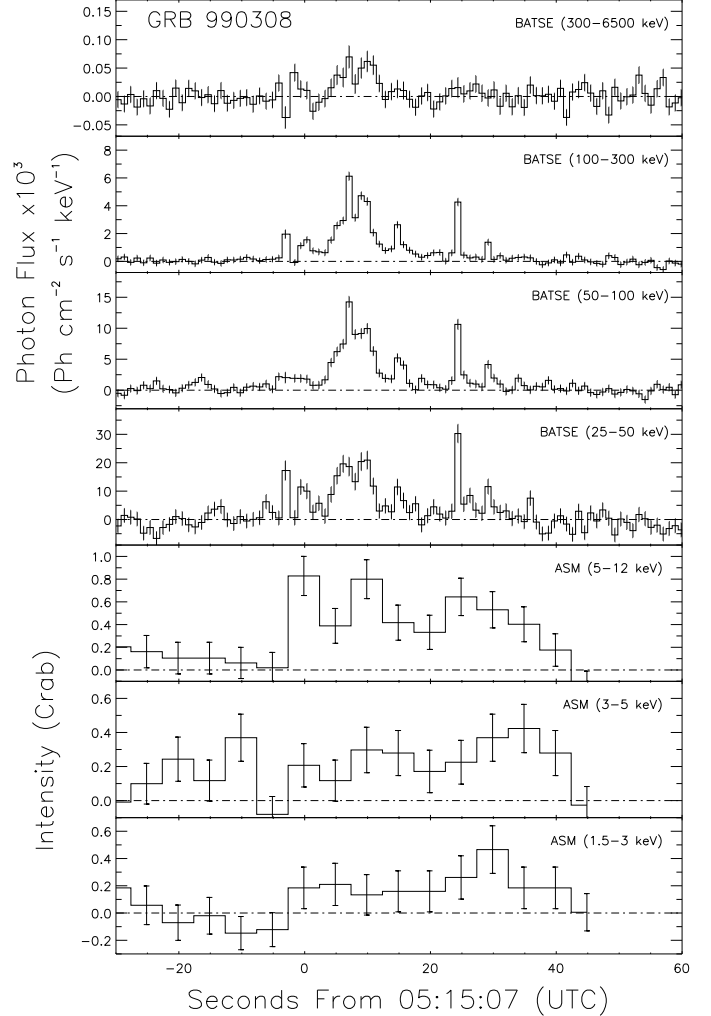


Fig. 16 – Time-series data for GRB 990308 in SSC 3 (5-s bins; 1.5–12 keV) and BATSE (1-s bins; 25–6500 keV).

set of the afterglow, the soft lag would be the result of the decay of  $\nu_m$  (see Eq. 2), which is predicted by the external shock model of Mészáros & Rees (1997) to fall as  $(t - t_0)^{-2/3}$ , where  $t$  is measured by a distant observer at rest with respect to the blast center and  $t_0$  is the initiation time, when  $\nu_m$  is infinite. There is a  $\sim 8$  s difference between the times when the third peak reached its maximum in the C band ( $E \sim 7$  keV) and the A band ( $E \sim 2.25$  keV) at  $t \sim 154$  s and 162 s, respectively. If this delay is due to the evolution of  $\nu_m$ , the shock that generated the third peak must have begun cooling at 152 s after the BATSE trigger time. We therefore use this time as  $t_0$  to model the subsequent evolution of the emission.

The decay curve of the third peak can be fit with a power-law model, such that  $F(t) \propto (t - t_0)^{-\beta}$ . All three ASM energy bands show a decay from the third peak consistent with  $\beta = 1.3 \pm 0.1$ . This achromatic decay is in marked contrast to the decay from GRB 970828, as described below, but it is consistent with the afterglow observations from other GRBs and the predictions of the external shock model (Mészáros & Rees 1997). X-ray afterglow curves have been measured for twenty-three GRBs that occurred prior to 1999 August, and the power-law in-

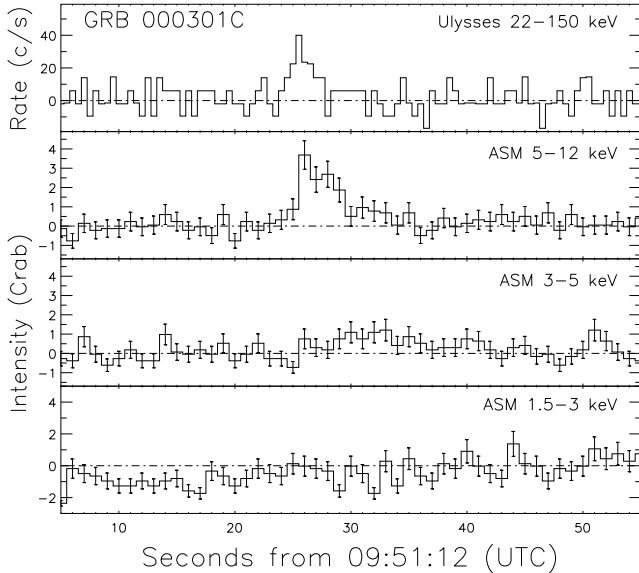


Fig. 17 – GRB 000301C as observed in SSC 2 (1-s bins; 1.5–12 keV) and the GRB detector on *Ulysses* (0.5-s bins; 22–150 keV). The rising count rate in the 1.5–3 keV channel indicates that the *RXTE* may be moving into a region of high activity in the Earth’s magnetosphere, or there may be interference from scattered Solar X-rays.

indices for the decay range from 1.1 for GRB 970508 (Piro et al. 1998b) to 1.57 for GRB 970402 (Nicastro et al. 1998). The decay from GRB 970815 is thus fully consistent with an afterglow-type decay. If one extrapolates this decay to the time of the *ASCA* follow-up observation,  $\sim 3.5 \times 10^5$  s after  $t_0$ , the predicted 2–10 keV flux of about  $8 \times 10^{-15}$  ergs  $\text{cm}^{-2}$   $\text{s}^{-1}$  lies below the *ASCA* upper limit of  $10^{-13}$  ergs  $\text{cm}^{-2}$   $\text{s}^{-1}$  (Murakami et al. 1997a). The lack of an *ASCA* detection thus does not rule out the possibility that the third peak is the start of an afterglow decay; neither does it support that interpretation.

An alternative scenario is that the third peak results from a shell catching up with the decelerating external shock; an early version of the enhancements seen late in the afterglow of other bursts, such as GRB 970508 (Piro et al. 1998b). This would indicate that whatever processes produce bursts continue to operate throughout the entire event. If this scenario is true, the afterglow and the burst cannot always be considered distinct events. It is possible, however, that the late pulses in the afterglow are not due to collisions from behind, as interpreted by Piro et al. (1998b), but instead are isolated instances of the remnant colliding with a dense patch of external medium.

GRB 970828 (Fig. 10) displays an extended interval of X-ray emission beyond the cessation of gamma-ray activity. As in the case of GRB 970815, we can ask if the ASM X-ray light curve reveals the onset of the X-ray afterglow. The final X-ray decay should then share temporal and spectral properties with X-ray afterglow observed at later times (Frontera et al. 2000). A power law decay curve, with the origin set at the BATSE trigger time, when fit to the 1.5–12 keV band data in the last ASM dwell, indicates that the flux decays as roughly  $t^{-5}$  (Fig. 18). All observed afterglow decay curves have indices between  $\sim 1.1$  and  $\sim 1.6$ , and the X-ray decay from this GRB was

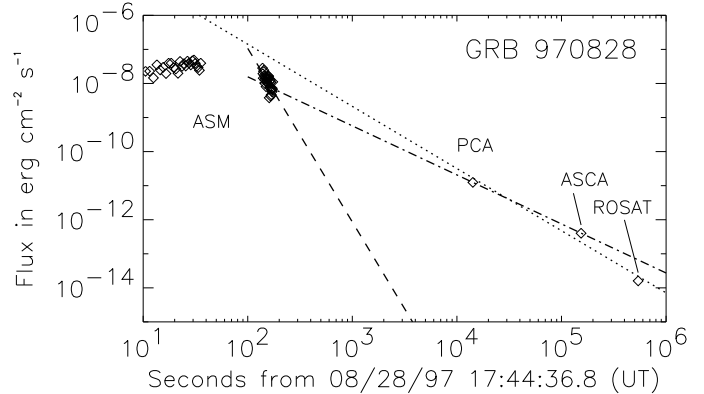


Fig. 18 – X-ray flux history of GRB 970828 ( $\sim 2$ –10 keV), as measured by the ASM, the PCA (Marshall et al. 1997), *ASCA* (Murakami et al. 1997b), and *ROSAT* (Greiner et al. 1997). The dashed line shows the best-fit power-law decay curve for the ASM data,  $F \propto t^{-5}$ . The dotted line shows the best-fit power-law for the three late-time flux measurements,  $F \propto t^{-0.5}$ . The *ROSAT* flux is derived by extrapolating the reported 0.5–2.4 keV spectrum out to 10 keV. If this extrapolation is excluded from consideration, the PCA and *ASCA* data are consistent with a power law decay of index 1.4 (Yoshida et al. 1998), shown here as a broken line.

measured by the PCA and *ASCA* over the following two days to decay as  $t^{-1.4}$  (Murakami et al. 1997b), as shown in Figure 18. There is nothing in the theory of external shocks to explain a decay index around 5 that later changes to 1.4. Although the assignment of  $t_0$  to the BATSE trigger time is somewhat arbitrary, the best-fit decay index is inconsistent with, and steeper than, a value of 1.4 for any value of  $t_0$ . We therefore find it unlikely that the ASM data represent the afterglow.

A fading X-ray afterglow was associated with GRB 980703 (Fig. 14) through observations with the *BeppoSAX* Narrow Field Instruments (NFI) 22 h after the event (Vreeswijk et al. 1999), and in contrast to GRB 970828, the tail of the ASM decay curve and the NFI flux measurements are consistent with a single power-law decay curve (Fig. 19). The best-fit decay index is  $\sim 1.3$ , a typical value for GRB afterglows. This value is consistent with the lower limit of 0.9 measured using only the NFI observations (Vreeswijk et al. 1999). The tail of the burst emission may therefore represent a transition to the afterglow. However, the large errors in the ASM measurements would allow the NFI flux measurements to vary by orders of magnitude and still appear consistent with a single decay. It is worth noting that the BATSE count rates reveal a second interval of emission from this burst, roughly 300 s after the onset of the event, at which time the burst position was outside the ASM FOV. The apparent connection between the decay from the first peak and the *BeppoSAX* afterglow is therefore likely a coincidence.

Even beyond these three examples, the X-ray flux from GRB events tends to be less variable and in almost all cases lasts longer than the associated gamma-ray flux. These increased peak widths may be examined in the context of synchrotron radiation theory. The cooling timescale for an electron undergoing synchrotron energy loss is inversely

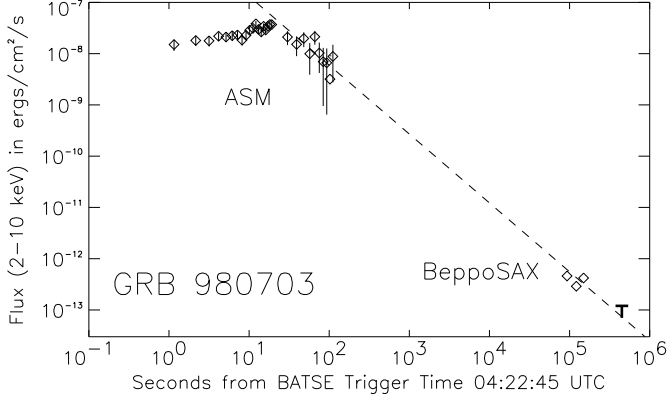


Fig. 19 – X-ray flux history of GRB 980703 ( $\sim 2-10$  keV), as measured by the ASM and the *BeppoSAX* NFI (Vreeswijk et al. 1999). The “T” shape indicates an upper limit. The dashed line shows the best-fit power-law decay curve combining both instruments,  $F \propto t^{-1.3}$ .

proportional to the electron’s Lorentz factor ( $t_c \propto 1/\gamma_e$ ). The synchrotron frequency of an emitting electron (and the characteristic photon energy  $E$  of the emitted radiation) goes as the square of its Lorentz factor ( $E \propto \gamma_e^2$ ). Hence, if a population of electrons is cooling through synchrotron radiation, one would expect to find the cooling time scales, or peak widths, to vary as  $E^{-1/2}$  (Rybicki & Lightman 1979; Piran 1999; Wijers & Galama 1999). Although geometric effects can extend the time over which a burst is visible to a distant observer, the relationship between the cooling time scale and the width of observed peaks in a GRB light curve is expected to be preserved (Piran 1999).

The fact that the bursts presented here were observed serendipitously by different instruments renders the width of the GRB peaks difficult to measure in many cases. The time resolution of the ASM MTS data, exacerbated by the relatively small effective area, also makes comparison of individual burst features problematic (*e.g.* Figs. 3 and 4). Nevertheless, we have measured peak widths as a function of energy band for seven bursts, and we display the results in Figure 20. Here, a peak width is estimated as the best-fit Gaussian function, with an uncertainty given by the  $2\sigma$  confidence interval for the Gaussian width. We also measured an exponential decay timescale, yielding equivalent results. For bursts with complex temporal structure, like GRB 970828 (Fig. 10) above 25 keV, a Gaussian function is an extremely poor match to the shape of the light curve, but we cite the best-fit Gaussian in order to compare duration consistently with the simpler bursts.

Figure 20 shows that only the simplest bursts are consistent with the prediction of synchrotron cooling. For example, the widths for GRB 000301C (Fig. 17), with a single-peaked Gaussian shape in both the ASM and *Ulysses* data, are consistent with the expected power-law solution with index of  $-0.5$  (Fig. 20h, dashed line). While GRB 960416 (Fig. 1) displayed multiple peaks, these peaks were widely separated, and the width of each peak is consistent with a  $E^{-1/2}$  scaling law (Fig. 20a & b). Again, the dashed line in the figure shows a representative power law with index  $-0.5$ .

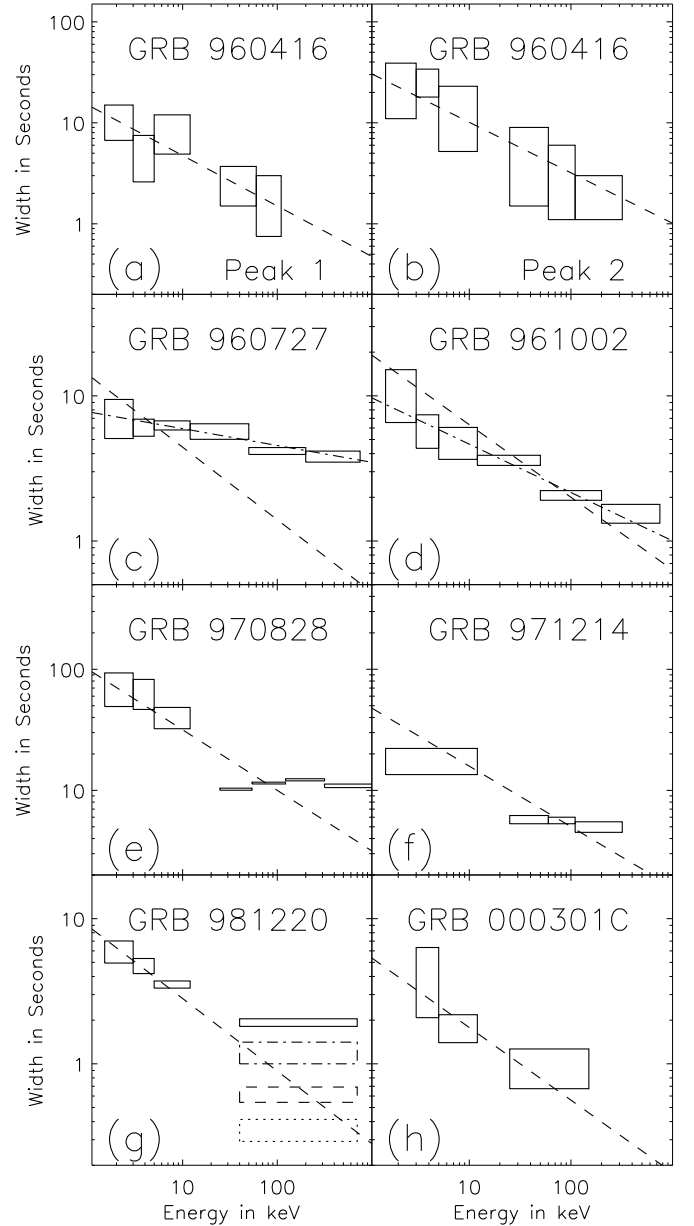


Fig. 20 – Peak width vs. energy for seven GRBs. The GRB modeled with a simple Gaussian function, and the  $\pm 2\sigma$  confidence interval for the width is plotted on the  $y$ -axis, against the appropriate energy channel. Data are from BATSE, the *BeppoSAX* GRBM, *Ulysses*, *Konus*, and the ASM. The dashed lines in each plot represent the  $E^{-0.5}$  dependence expected from synchrotron cooling. The broken lines in panels (c) and (d) indicate the best-fit slopes.

Such a simple model, however, does not fit any of the other bursts. GRB 960727 (Fig. 3) and GRB 961002 (Fig. 4) seem simple as recorded by the ASM, but the *Konus* light curves reveal complex temporal structure. The total duration of both these bursts has a much flatter dependence on energy than synchrotron cooling would predict; the best-fit power law indices are inconsistent with a slope of  $-0.5$  (Compare the broken and dashed lines in Figures 20c and d). GRB 981220 (Fig 15) also displayed a simple, single-peaked structure in the ASM time-series

data, but the *BeppoSAX* count rates resolve this into three narrower peaks at high energies. The ASM data alone are consistent with a power law index of  $-0.5 \pm 0.1$  (Fig. 20g), but the extrapolation of this scaling law to the energy range of the *BeppoSAX* GRBM is inconsistent with the measured width of the peak as modeled by a single Gaussian (the solid box spanning the 40–700 keV range). However, if the GRBM light curve is modeled by the superposition of three Gaussian events, then their widths are (in chronological order)  $0.35 \pm 0.1$  s,  $0.6 \pm 0.1$  s, and  $1.2 \pm 0.2$  s (shown as the dotted, dashed, and broken boxes, respectively). These three boxes are all consistent with the extrapolated power-law, and perhaps the emission seen in soft X-rays is dominated by the cooling of a single shock that produced one of these high-energy peaks.

The widths of the ASM light curves for GRB 970828 (Figs. 10 & 20e) and GRB 971214 (Figs. 13 & 20f) do not match well with an extrapolation of the primary peak width as observed by BATSE. In both cases, the BATSE light curves showed multiple peaks of emission, and a Gaussian model of the primary peak widens much more slowly than a  $E^{-0.5}$  power law would predict. Within the context of the internal shock model, the extended length of the ASM light curve for GRBs 970828 and 971214 can perhaps be interpreted as the reheating of the matter heated by the initial shock, which does not have time to cool in the X-ray regime before it is shocked again. However, there is no reason why the multiple shocks would necessarily be shocking the same electrons. This scenario also would not explain the smaller indices for GRBs 960727 and 961002 (Fig. 20c & d).

In short, only the simplest bursts display the  $E^{-0.5}$  dependence of width on energy predicted by synchrotron cooling. We point out that the only other burst for which this hypothesis has been tested across X-ray and gamma-ray bands, GRB 960720, was also a simple burst with a single peak (Piro et al. 1998a). A likely explanation of this discrepancy is that multiple peaks are indicative of complex interactions that violate the assumption of a single infusion of energy followed by cooling through radiation. It is unclear why some complex bursts lead to abnormally long soft X-ray light curves (such as GRB 970828), while others (like GRB 960727) show a much weaker dependence on energy. It is possible that individual peaks in these complex bursts do behave consistently with the predictions of synchrotron cooling, as do the well-separated peaks in GRB 960416 and perhaps the short peaks in GRB 981220, but most often, the statistics and time resolution of the ASM data do not allow us to track the behavior of individual short peaks.

When study of individual peaks is possible, however, several show a soft lag in their times of maximum count rate. It is worth noting that several do not, at least within the limitations of the effective time resolution. In no case did we observe any candidate for a distinct X-ray precursor, such as that associated with GRB 980519 (in 't Zand et al. 1999) or perhaps GRB 900126 (Murakami et al. 1991). Precursor events are rare, so their absence in the ASM sample is unsurprising.

What is perhaps surprising is the absence of GRBs shorter than 10 s in duration. The GRBs in the BATSE catalog have a well-known bimodal duration distribution

with peaks at 0.1 s and 10 s (Hurley 1992; Kouveliotou et al. 1993; Fishman et al. 1994; Koshut et al. 1996). Our variability search was conducted on time-scales of 1/8 s, 1 s, and 9 s, and yet all the GRBs we found are drawn from the longer sub-population, although GRB 000301C is a borderline case (Jensen et al. 2001). If the typical peak intensities of the short bursts are of the same magnitude as or less than those of the long bursts, the ASM is less likely to detect the short bursts, although a short burst should still stand out in the time-series data. Our search was able to detect the short bursts from SGR 1627–41 (Smith, Bradt & Levine 1999). The population of short bursts represents roughly 25% of the first BATSE GRB catalog (Kouveliotou et al. 1993), so perhaps the absence of short GRB events in the ASM sample is a statistical fluctuation, but it is noteworthy that all of the bursts localized to date by the *BeppoSAX* WFC have also been from the population of longer bursts (Gandolfi et al. 2000; Frontera et al. 2000). The BATSE data suggest that the shorter bursts have harder spectra, so perhaps they are not bright enough in the 1.5–12 keV range for ASM detection.

This project combined results from several instruments, and hence could not have been completed without the help of many individuals. Of crucial help was Scott Barthelmy's work in creating and maintaining the GCN. We would also like to acknowledge the support of the *RXTE* team at MIT and NASA/GSFC. Support for this work was provided in part by NASA Contract NAS5–30612. D. A. Smith is supported by NSF fellowship 00-136. KH is grateful for Ulysses and IPN support under JPL Contract 958056 and NASA grants NAG 5–9503 and NAG 5–3500.

## REFERENCES

- Aptekar, R., et al. 1995, *Space Science Reviews*, 71, 265
- Band, D., et al. 1993, *ApJ*, 413, 281
- Blandford, R. & McKee, C. 1976, *Phys. Fluids*, 19, 1130
- Bradt, H., Levine, A., Marshall, F., Remillard, R., Smith, D., & Takeshima, T. 2001, in "Gamma-Ray Bursts in the Afterglow Era: 2nd Workshop", ed. F. Frontera, E. Costa, & J. Hjorth, (Springer Verlag: New York), in press (astro-ph/0108004)
- Cavallo, G. & Rees, M. J. 1978, *MNRAS*, 183, 359
- Connors, A. & Hueter, G. J. 1998, *ApJ*, 501, 307
- Costa, E. et al. 1997, *Nature*, 387, 783
- Feroci, M., et al. 1997, in *SPIE Conference Proceedings*, ed. Siegmund & Gummin, Vol. 3114, 186 (astro-ph/9708168)
- Golenetskii, S., Mazets, E., Aptekar, R., & Ilinskii, V. 1983, *Nature*, 306, 451
- Fenimore, E. E., Madras, C. D., & Nayakshin, S. 1996, *ApJ*, 473, 998
- Fishman, G. J., et al. 1994, *ApJS*, 92, 229
- Ford, L., et al. 1995, *ApJ*, 439, 307
- Frontera, F., Costa, E., dal Fiume, D., Feroci, M., Nicastro, L., Orlandini, M., Palazzi, E., & Zavattini, G. 1997, *A&AS*, 122, 357
- Frontera, F. et al. 2000, *ApJS*, 127, 59
- Gandolfi, G. et al. 2000, in *Proc. 5th Huntsville Gamma-Ray Burst Symp.*, ed. R. M. Kippen, R. S. Mallozzi, & G. J. Fishman (New York: AIP), 23 (astro-ph/0001011)
- Giblin, T. W., van Paradijs, J., Kouveliotou, C., Connaughton, V., Wijers, R. A. M. J., Briggs, M. S., Preece, R. D., & Fishman, G. J. 1999, *ApJ*, 524, L47
- Goodman, J. 1986, *ApJ*, 308, L47
- Greiner, J., Schwarz, R., Englhauser, J., Groot, P., & Galama, T. 1997, *IAU Circ. No. 6757*
- Hurley, K. 1992, in *AIP Conf. Proc. 265, Gamma-Ray Bursts*, ed. W. Paciesas & G. Fishman (New York: AIP), 3
- Hurley, K., et al. 1992, *A&AS*, 92, 401
- in 't Zand, J. J. M., Heise, J., van Paradijs, J., & Fenimore, E. E. 1999, *ApJ*, 516, L57
- Jensen, B. L. et al. 2001, *A&A*, 370, 909
- Kobayashi, S., Piran, T., & Sari, R. 1997, *ApJ*, 490, 92
- Kobayashi, S., Piran, T., & Sari, R. 1999, *ApJ*, 513, 669
- Kobayashi, S., & Sari, R. 2001, *ApJ*, 551, 934
- Koshut, T. M., Paciesas, W. S., Kouveliotou, C., van Paradijs, J., Pendleton, G. N., Fishman, G. J., & Meegan, C. A. 1996, *ApJ*, 463, 570
- Kouveliotou, C., Meegan, C. A., Fishman, G. J., Bhat, N. P., Briggs, M. S., Koshut, T. M., Paciesas, W. S., & Pendleton, G. N. 1993, *ApJ*, 413, L101
- Laros, J. G., Evans, W. D., Fenimore, E. E., Klebesadel, R. W., Shulman, S., & Fritz, G. 1984, *ApJ*, 286, 681
- Levine, A. M., Bradt, H., Cui, W., Jernigan, J. G., Morgan, E. H., Remillard, R., Shirey, R. E., & Smith, D. A. 1996, *ApJ*, 469, L33
- Lloyd, N. & Petrosian, V. 2000, *ApJ*, 543, 722
- Marshall, F., Cannizzo, J., & Corbet, R. 1997, *IAU Circ. No. 6727*
- Mazets, E. P., et al. 1981, *Ap. Space Sci.*, 80, 3
- Mészáros, P. & Rees, M. 1992, *ApJ*, 397, 570
- Mészáros, P. & Rees, M. 1997, *ApJ*, 476, 232
- Metzger, A. E., Parker, R. H., Gilman, D., Peterson, L. E., & Trombka, J. I. 1974, *ApJ*, 194, L19
- Murakami, T., et al. 1989, *PASJ*, 41, 405
- Murakami, T., Inoue, H., Nishimura, J., van Paradijs, J., & Fenimore, E. E. 1991, *Nature*, 350, 592
- Murakami, T., Ueda, Y., Ishida, M., Fujimoto, R., Yoshida, A., & Kawai, N. 1997, *IAU Circ. No. 6722*
- Murakami, T., Ueda, Y., Yoshida, A., Kawai, N., Marshall, F., Corbet, R., & Takeshima, T. 1997, *IAU Circ. No. 6732*
- Narayan, R., Paczyński, B., & Piran, T. 1992, *ApJ*, 395, L83
- Nicastro, L. et al. 1998, *A&A*, 338, L17
- Norris, J. P., Share, G. H., Messina, D. C., Dennis, B. R., Desai, U. D., Cline, T. L., Matz, S. M., & Chupp, E. L. 1986, *ApJ*, 301, 213
- Ogasaka, Y., Murakami, T., Nishimura, J., Yoshida, A., & Fenimore, E. E. 1991, *ApJ*, 383, L61
- Pendleton, G. N., et al. 1994, *ApJ*, 431, 416
- Pendleton, G. N., et al. 1996, *ApJ*, 464, 606
- Pendleton, G. N., et al. 1997, *ApJ*, 489, 175
- Piran, T. 1999, *Phys. Rep.*, 314(6), 575 (astro-ph/9810256)
- Piro, L., et al. 1998, *A&A*, 329, 906
- Piro, L. et al. 1998, *A&A*, 331, L41
- Preece, R. D., Briggs, M. S., Mallozzi, R. S., Pendleton, G. N., Paciesas, W. S., & Band, D. L. 2000, *ApJS*, 126, 19
- Rees, M. & Mészáros, P. 1992, *MNRAS*, 258, 41
- Remillard, R., Wood, A., Smith, D., & Levine, A. 1997, *IAU Circ. No. 6726*
- Rybicki, G. & Lightman, A. 1979, *Radiative Processes in Astrophysics* (New York: John Wiley & Sons)
- Sari, R. 1997, *ApJ*, 489, L37
- Sari, R., Narayan, R., & Piran, T. 1996, *ApJ*, 473, 204
- Sari, R. & Piran, T. 1999, *ApJ*, 485, 270
- Sari, R. & Piran, T. 1999, *ApJ*, 520, 641
- Sari, R., Piran, T., & Narayan, R. 1998, *ApJ*, 497, L17
- Sazonov, S. Y., Sunyaev, R. A., Terekhov, O. V., Lund, N., Brandt, S., & Castro-Tirado, A. J. 1998, *A&AS*, 129, 1
- Schaefer, B. et al. 1999, *ApJ*, 524, L103
- Shemi, A. & Piran, T. 1990, *ApJ*, 365, L55
- Smith, D. 1999, PhD dissertation, Massachusetts Institute of Technology
- Smith, D. A., et al. 1999, *ApJ*, 526, 683
- Smith, D. A., Bradt, H. V., & Levine, A. M. 1999, *ApJ*, 519, L147
- Smith, D. A., Hurley, K., & Cline, T. 2000, *GCN Circ. No. 568*
- Seward, F. 1978, *Journal of the British Interplanetary Society*, 31, 83
- Strohmayr, T. E., Fenimore, E. E., Murakami, T., & Yoshida, A. 1998, *ApJ*, 500, 873
- Trombka, J. I., Eller, E. L., Schmadebeck, R. L., Adler, I., Metzger, A. E., Gilman, D., Gorenstein, P., & Bjorkholm, P. 1974, *ApJ*, 194, L27
- Vreeswijk, P. et al. 1999, *ApJ*, 523, 171
- Wheaton, W. A., et al. 1973, *ApJ*, 185, L57
- Wijers, R. & Galama, T. 1999, *ApJ*, 523, 177
- Yoshida, A., Namiki, M., Otani, C., Kawai, N., Murakami, T., Ueda, Y., Shibata, R., & Uno, S. 1998, in *AIP Conf. Proc. 428, Gamma-Ray Bursts*, ed. C. Meegan, R. Preece, & T. Koshut (New York, AIP), 441